Comparison of Methods for Determining Boundaries of Lipid Patches in a Phase Separation Problem on a Torus

D. Miller and M. Barg

Abstract - Determining lipid configurations on a curved surface in a phase separation problem is a problem that has gained interest in the mathematical biology community recently. We consider the case in which two different lipid types are present, and we locate lipid patch boundaries to understand the lipid configurations. While a variety of methods can be used to solve such problems, we actually compare two different methods in this work: a diffuse interface approach and an initial value problem approach. In the latter approach, we directly compute, albeit approximately, the patch boundary curve on a ring torus. Solving numerically, we find good agreement between the two methods and provide results that relate different parameters from the two approaches.

Keywords : phase separation; interface; Canham-Helfrich functional

Mathematics Subject Classification (2020) **:** 74A50; 65D17

1 Introduction

This work contributes to the ongoing effort to model lipid domain formation on curved biological surfaces by rigorously comparing two paradigms: the diffuse interface approach and the initial value problem (IVP) approach. While both methodologies are grounded in the thermodynamic and geometric principles of membrane biophysics, they differ in how they represent phase boundaries. The current literature provides theoretical and numerical treatments of each method independently, ranging from phase field models on curved surfaces [8], [17] to Euler–Lagrange equations derived from variational principles [11], [12], [15]. Comparative analyses of these approaches on biologically relevant geometries, such as the torus, remain under-explored. We focus solely on the (R, r)-ring torus

$$(x^2 + y^2 + z^2 + R^2 - r^2)^2 - 4R^2(x^2 + y^2) = 0$$

with $R = 2$ and $r = 1$ in this work.

By aligning and contrasting solutions generated by these two approaches, particularly in cases where a so-called conservation constraint is small and rotational symmetry leads to multiple local minimizers, this work highlights a connection between the two approaches and can therefore be expected to deepen our understanding of lipid organization. The

analytical insights of Gillmor, Ren, and Lee, in [11], regarding the role of Gauss curvature are tested here with an independent differential equation (DE) from [10] that can be solved to provide a curve as the interface between the lipid types. This provides further validation to both minimization-based schemes.

Cell membranes are fundamental to life, acting as dynamic interfaces that not only define cell boundaries, but also orchestrate transfer of signals and regulate the transport of molecules and energy. In nearly all living organisms, cell membranes consist of a bilayer of phospholipid molecules that are mostly free to diffuse through the membrane surface, in what is described as a fluid-mosaic model. Recent studies demonstrate that lipid bilayers are far from homogeneous; rather, in certain environmental scenarios, the molecules spontaneously segregate into spatially distinct regions of different lipid phases, including a liquid-disordered phase (typically making up the majority of the cell surface), and a liquid-ordered phase (which makes up structural rafts).

Imaging techniques have revealed such self-organization (see, e.g, [4]). Physical properties of the cell have been found to play a role in how membrane curvature interacts with a line tension at domain boundaries, and this interplay influences both the size and location of lipid patches. The different patch phases are known to have different physical properties, such as surface tension, bending rigidity, and Gaussian rigidity. Seeking to mathematically model biophysical reasons for the biconcave disk shape of red blood cells, P.B. Canham developed a free energy model [6] which was refined by W. Helfrich, who expanded the theory to general lipid bilayers and proposed experimental pathways for testing it. The Canham-Helfrich free energy model shows that membrane heterogeneity is not merely a biochemical property, but a mechanical and energetic one as well, governed by the physical principles of soft matter physics.

More specifically, a generalized, constrained Canham-Helfrich model is an energy functional

$$F = \sum_{\alpha=\pm} \int_{M_\alpha} dA(\lambda_\alpha + k_\alpha H^2 + \bar{k}_\alpha K) + \sigma \int_\Gamma ds \tag{1}$$

that includes the membrane's mean curvature H, Gauss curvature K, and interfacial line tension σ. In Eq. (1), the subscript α refers to one of the two different lipid types and $M = M_+ \cup M_-$ is a mathematical surface representing the biological membrane. As in much of the related literature, M is taken to be a compact surface without boundary. The boundary between M_+ and M_- is denoted by Γ. It may be the case that Γ consists of many closed curves (see, e.g., [1]). In this work, we assume the environmental conditions and subsequent parameter values in Eq. (1) are such that Γ is a single closed curve. We refer to Γ as the interface curve. The constant parameters $k_\pm$ and $\bar{k}_\pm$ are bending and Gaussian rigidities, respectively, and $\lambda_\pm$ are Lagrange multipliers that enforce surface area constraints. Considering the functional in a variational framework allows one to predict equilibrium shapes. One seeks solutions to the minimization problem

$$\text{Problem } P_1 \qquad\qquad \inf F \tag{2}$$

where the infimum is taken over a suitable collection of lipid configurations. By working directly with the corresponding Euler–Lagrange equation derived from F, researchers

can describe the stable configurations of the membrane as solutions to nonlinear ordinary differential equations (see, e.g., [15]). Together, these constraints and theoretical principles provide a foundation for understanding lipid domain formation serving as a bridge between membrane biophysics and mathematical modeling. In this work, we produce numerical solutions to the Euler-Lagrange equation and consider the resulting set of points $E(P_1)$ to be the interfacial "curve" between distinct lipid regions.

A significant strand of work in modeling phase separation and lipid domain formation has been the development of a diffuse interface method, which aims to capture the energetics and dynamics of interfaces without explicitly tracking sharp boundaries. This approach emerged as a powerful tool for studying biological membranes, particularly when lipid composition varies smoothly across space. Using density functional theory with the aim of modeling diblock copolymers, Choksi and Ren, in [7], derived an effective free energy functional to describe microphase separation, where competing short and long-range interactions lead to modulated structures (see also [16]), an idea that foreshadowed similar behaviors in lipid bilayers. Their work helped justify the use of non-local and higher-order terms in diffuse interface energies, laying a conceptual foundation for later biological applications [11]. Wang and Du, in [17], introduced a diffuse interface model on curved surfaces to simulate phase separation on biomembranes. Their formulation used two phase functions instead of the previous works which only used one. Elliott and Stinner, in [8], put the phase field methodology on firm theoretical ground. Their work helped reconcile the phase field description with the Euler-Lagrange equations of the Canham-Helfrich bending energy. This marked a major step toward models capable of reproducing both the shape transformations and compositional heterogeneity observed in biological membranes.

Building upon these foundational models, more recent work has focused on a numerical aspect of the diffuse interface approach. Barg and Mangum, in [2], have contributed to this development by extending earlier numerical efforts such as those of Baginski et al. [9] through the implementation of the finite element method for solving a so-called diffuse interface energy minimization problem. A key contribution of their work lies in the effort to define an interface boundary between lipid domains in a precise and reproducible way. This is critical in the context of biological membranes, where domain boundaries often play functional roles and need to be quantitatively compared across models. Their approach allows one to compare a boundary produced from the diffuse interface method to $E(P_1)$. In this framework, the interface is selected from a diffuse transition zone in the phase field and computed as a curve, $E(P_2)$, enabling comparison between solutions derived from different modeling perspectives. This dual viewpoint could provide a framework for analyzing solution stability, patch shape, and patch location in various surface geometries. Explicitly, [2] sets up the diffuse interface approach in the following way. Let the surface M represent the lipid bilayer. Consider a minimization problem, denoted

$$\text{Problem } P_2 \qquad \inf_{\xi \in \mathcal{A}} F_p(\xi) \tag{3}$$

Here, $\mathcal{A}$ is a space of admissible functions, $\xi : M \to \mathbb{R}$ is a phase function, and $F_p(\xi)$ is

the well-known Landau-type free energy functional

$$F_p(\xi) = \int_M \frac{\epsilon^2}{2}||\nabla\xi||^2 + \beta\xi^2(1-\xi)^2 \, dS$$

where $\epsilon > 0$ and $\beta > 0$ are constants, ∇ is a surface gradient, and dS is surface area measure. We note that the phase function $\xi(x, y, z)$ represents the density of one particular lipid type at $(x, y, z) \in M$, which yields $0 \leq \xi \leq 1$. See [2] for further details about F_p. The space of admissible functions includes the linear conservation constraint

$$\int_M \xi \, dS = \omega|M| \tag{4}$$

where $|M|$ is the surface area of M and ω is a conservation constraint parameter with $0 < \omega < 1$.

Working with a phase field energy functional derived from the Canham-Helfrich-type bending energy, Gillmor, Ren, and Lee, in [11], demonstrated that when ω is sufficiently small, a minimizing configuration tends to be a geodesic disk, centered near points of maximum Gauss curvature on the surface. On the (R, r)-torus, such curvature maxima occur along the so-called "large equator" defined by $x^2+y^2 = (R+r)^2$, which implies that multiple energetically equivalent configurations can emerge, each centered near a different point along this high-curvature curve [11]. This multiplicity of solutions reflects an intrinsic rotational degeneracy in the system, where the phase field can rotate about the z-axis or a nearby axis without a significant change in total energy. As a result, when comparing computed solutions, it becomes essential to account for rotational alignment. For this, one popular technique is that of the Kabsch algorithm [14], a well-established method for computing the optimal rotation matrix that minimizes the root-mean-square deviation (RMSD) between two configurations of points. Originally introduced in crystallography to align molecular structures [14], the Kabsch algorithm ensures meaningful comparisons between configurations that differ only by a rigid body motion. Another technique is to use a matrix called the Rodrigues rotation matrix (see [5]). To guarantee that rotated points remain on M, we will use a standard rotation matrix for a rotation around the z-axis in Section 3.2.

In this work, we treat $E(P_2)$ as a given quantity. Then, exploration into the initial value problem approach is necessary (see Section 2.3). In our work, one must choose a surface to parametrize and use that parametrization, along with other constraints, to write the appropriate DEs in a nice form. This will be done by using the differential equations presented in [10], along with observations made about the geometry of the system. In the end, an IVP will be solved using MATLAB's *ode45* solver (see Section 3), giving a numerical solution as the boundary curve $E(P_1)$. As noted in [10], analytical solutions only exist for simple geometries. The overall question being answered here is this: "How similar are solutions to the phase separation problem from the diffuse interface and IVP approaches?" In order to provide an answer, distances between $E(P_1)$ and $E(P_2)$ will be computed in Section 3.3.

This work will be of interest to applied mathematicians, biophysicists, and computational scientists who seek to understand how geometry, topology, and physical constraints interplay in soft matter systems. From a mathematical perspective, the comparison enriches the toolkit for phase separation problems on surfaces, connecting variational methods, numerical DEs, and geometric analysis. From a biological modeling standpoint, understanding where and how lipid domains form has implications for membrane signaling, trafficking, and curvature-driven processes in living cells [4],[13],[16]. This project demonstrates a synthesis of theoretical modeling, numerical implementation, and applied analysis, a cross-disciplinary blend reflective of contemporary mathematical biology. It advances the modeling conversation by not only applying known techniques but by testing their assumptions, comparing their outcomes, and proposing computational tools that can be generalized to other systems. This work is important in an era where biological complexity increasingly calls for mathematical clarity.

2 Producing $E(P_1)$ and $E(P_2)$

This section provides details for how the sets $E(P_1)$ and $E(P_2)$ arise from Problem P_1 and Problem P_2, respectively. We begin with a brief discussion about $E(P_2)$. As mentioned above, we treat $E(P_2)$ as a given input in this work, and we refer the interested reader to [2] and the references therein for more details about producing $E(P_2)$ as a solution to Problem P_2.

2.1 Diffuse Interface Approach for $E(P_2)$

A solution of Problem P_2 from [2] is what is called the diffuse interface solution in this work. Formulating Problem P_2 with the given constraints and a chosen surface M, it is possible to solve for the boundary of a patch. A graph of the solution curve can be produced upon the completion of this approach. The following is an example of a solution that could be obtained from executing the diffuse interface approach, where M is the $(2,1)$-torus with the equation of $(x^2+y^2+z^2+3)^2 = 16(x^2+y^2)$. This example uses a conservation constraint $\omega = 0.05$, and M is approximated with a faceted surface using 16,064 triangles and 8,032 nodes. As in the literature, the parameter $\epsilon \approx 0.0535$ is selected to be one-half of the average edge length of a triangle and $\beta = 0.25$. The boundary of the solution is selected to be those nodes that are a fixed geodesic distance from a center of the patch. In Figure 1, the magenta region consists of points where $\xi > 0.75$ and the blue region consists of points where $\xi \leq 0.75$. The blue curve is $E(P_2)$, the estimated boundary curve for the surface patch where the two different lipids meet. This is one approach to calculating these solution patches, but the IVP method could also be used to calculate them. We choose to use $\xi = 0.75$ as a "cut-off" phase value for solution patch membership in order to be consistent with the literature (see, e.g., [2] or [3]). We note that [3] provides some justification for this cut-off value in terms of solution patch areas. We refer to $E(P_2)$ as a curve, but it is a discrete set of 576 points that are selected to be uniformly distributed around the patch boundary. In the following, images of the

curves $E(P_2)$ and $E(P_1)$ are produced in MATLAB which interpolates with straight line segments between consecutive points in the ordered sets $E(P_2)$ and $E(P_1)$. While we refer to the sets as curves, we do not use any of the interpolated points in our measurements for distances between the sets.

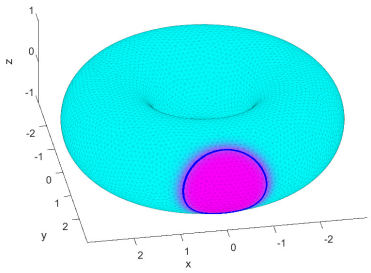

Figure 1: Solution patch and $E(P_2)$ from the diffuse interface approach with $\omega = 0.05$.

2.2 The IVP Approach for $E(P_1)$

As explained in [10], we consider an axisymmetric surface for the IVP approach. An axisymmetric surface (i.e., surface of revolution) is created by revolving a generating curve around the z-axis through a rotation angle denoted by ϕ (see [10, Fig. 4]). For certain generating curves, this gives the curvature of the geometry to be non-uniform while still being symmetric. An axisymmetric surface can be parameterized by

$$\mathbf{r}(t, \phi) =< r(t)\cos(\phi), r(t)\sin(\phi), z(t) >$$

where t is the arc-length along the generating curve, $\phi \in [0, 2\pi]$, and $r(t)$ and $z(t)$ are real-valued functions. The angle between the meridional direction $\mathbf{k}_1$ and the r-axis is $\psi = \psi(t) = \arctan\left(\frac{dz}{dt}/\frac{dr}{dt}\right)$ (see Fig. 2(a)).

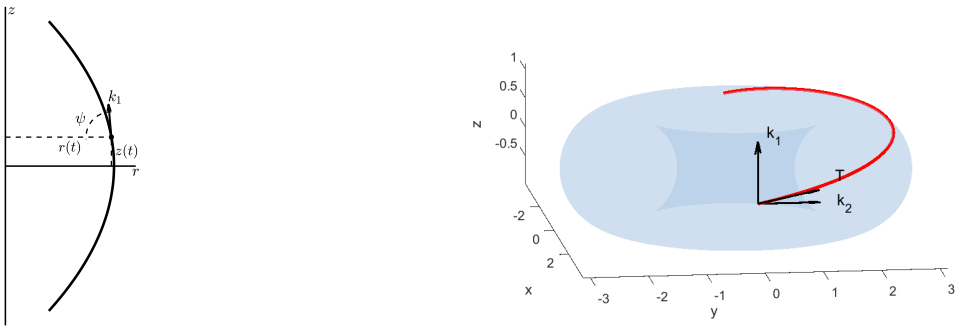

(a) The generating curve as in [10, Fig. 4].

(b) Interface curve as in [10, Fig. 4].

Figure 2: Generating curve and $E(P_1)$ schematic in red.

The formulas in [10, Eq. 20] for the mean and Gauss curvature of a surface of revolution are given here in Eq. (5):

$$H = -\frac{1}{2}\frac{d\psi}{dt} - \frac{\sin(\psi)}{2r}, \quad K = \frac{\sin(\psi)}{r}\frac{d\psi}{dt} \tag{5}$$

The derivation of H and K in Eq. (5) will be done in Appendix A. With these expressions for H and K, [10] creates its main differential equation, which is used as the general interface equation for the surface of revolution. This DE from [10, Eq. 24], is

$$\frac{1}{r}\frac{d}{dt}\left[r\sin\theta + \left(\frac{\Delta\bar{\kappa}}{\sigma} + \frac{\Delta\kappa}{2\sigma}\right)\cos\psi\right] = \frac{\Delta\kappa}{4\sigma}\left[\left(\frac{d\psi}{dt}\right)^2 + \frac{\sin^2\psi}{r^2}\right] + \frac{\Delta\lambda}{\sigma} \tag{6}$$

where $\Delta\kappa = k_+ - k_-, \Delta\bar{\kappa} = \bar{k}_+ - \bar{k}_-$, and $\Delta\lambda = \lambda_+ - \lambda_-$. In Eq. (6), θ is the angle between the interface's unit tangent vector $\mathbf{T}$ and the meridional direction vector $\mathbf{k}_1$ (see Fig. 2(b)).

It is from this differential equation, along with a chosen parametrization, that we produce the boundary curve of a patch $E(P_1)$. The solution depends on specific constants which will be discussed in Section 2.3. However, in [10], solution curves were shown for a corrugated cylinder using these constants. Such solution curves can be seen in [10, Fig. 5]. Following [10], we write $\eta_k = \frac{\Delta\kappa}{L\sigma}$ and $\eta_{\bar{k}} = \frac{\Delta\bar{\kappa}}{L\sigma}$, where $L = \max_t\{r(t)\}$ is the characteristic length of the system. This will be used to help determine the values for the constants in order to get a solution curve on the parameterized surface.

2.3 Derivation of the General Initial Value Problem

This section is centered around the application of the discussion in Section 2 to the problem of comparing the boundary curve from the diffuse interface approach with the boundary curve from our solution to the IVP approach. We provide details from the approach in [10] along with further work with the IVP approach. The boundary curve Γ is parametrized by $\Gamma(s) = \mathbf{r}(t(s), \phi(s))$ where s is the arc-length along Γ. We first treat s as a (local) function of t. This relationship occurs because position along the boundary curve corresponds to position along the generating curve and vice versa. Since the same value of t will correspond to different values of s, in order to produce a full boundary curve, we will reparametrize in Section 2.4 by treating $t = t(s)$ instead of $s = s(t)$.

One of the differential equations for the IVP comes from Equation (6). For ease of exposition, let $k_1 = \frac{\Delta\bar{\kappa}}{\sigma} + \frac{\Delta\kappa}{2\sigma}, k_2 = \frac{\Delta\kappa}{4\sigma}$, and $k_3 = \frac{\Delta\lambda}{\sigma}$. Now, Equation (6) is

$$\frac{1}{r}(r\sin\theta + k_1\cos\psi)' = k_2\left((\psi')^2 + \frac{\sin^2\psi}{r^2}\right) + k_3 \tag{7}$$

where $' = \frac{d}{dt}$. Since

$$r' = \cos\psi, \quad z' = \sin\psi, \quad \frac{z''}{\cos\psi} = \psi'$$

(see Fig. 2(a)), we can substitute into Eq. (7) to obtain

$$\frac{1}{r}(r\sin\theta + k_1 r')' = k_2\left(\frac{(z'')^2}{(r')^2} + \frac{(z')^2}{r^2}\right) + k_3$$

Solving for θ' yields

$$\theta' = \frac{1}{\cos\theta}\left[k_2\left(\frac{(z'')^2}{(r')^2} + \frac{(z')^2}{r^2}\right) + k_3 - \frac{r'\sin\theta - k_1 r''}{r}\right] \tag{8}$$

The second differential equation for the IVP is an equation for $\frac{d\phi}{dt}$. The boundary curve $\Gamma(s) = \mathbf{r}(t(s), \phi(s))$, parameterized by the arc-length s, is in the surface. Its unit tangent vector is

$$\mathbf{T} = \mathbf{r}_t\frac{dt}{ds} + \mathbf{r}_\phi\frac{d\phi}{ds}$$

where $\mathbf{r}_t = \frac{\partial \mathbf{r}}{\partial t}$ and $\mathbf{r}_\phi = \frac{\partial \mathbf{r}}{\partial \phi}$. Since the direction of $\mathbf{r}_t$ coincides with the direction of $\mathbf{k}_1$, we have that θ is the angle between $\mathbf{T}$ and $\mathbf{r}_t$. Then

$$\cos\theta = \mathbf{r}_t \cdot \left(\mathbf{r}_t\frac{dt}{ds} + \mathbf{r}_\phi\frac{d\phi}{ds}\right) = \mathbf{r}_t \cdot \mathbf{r}_t\frac{dt}{ds} + \mathbf{r}_t \cdot \mathbf{r}_\phi\frac{d\phi}{ds} = \frac{dt}{ds}$$

Since

$$1 = ||\mathbf{T}||^2 = \left|\left|\mathbf{r}_t\frac{dt}{ds} + \mathbf{r}_\phi\frac{d\phi}{ds}\right|\right|^2 = \left(\frac{dt}{ds}\right)^2 + r^2\left(\frac{d\phi}{ds}\right)^2 = \cos^2\theta + r^2\left(\frac{d\phi}{ds}\right)^2$$

we find

$$\frac{d\phi}{ds} = \frac{|\sin\theta|}{r}$$

and therefore

$$\frac{d\phi}{dt} = \frac{d\phi}{ds}\frac{ds}{dt} = \frac{|\sin\theta|}{r\cos\theta} \tag{9}$$

For parametrizing the torus, we use the functions

$$r(t) = 2 + \sin(t) \quad \text{and} \quad z(t) = -\cos(t) \tag{10}$$

Computing r', z', r'', and z'' and plugging into Eq. (8) yields

$$\theta' = f(t,\theta) = \frac{k_2 + k_3}{\cos\theta} + \frac{k_2\sin^2 t}{(2+\sin t)^2\cos\theta} + \frac{k_1\sin t}{(2+\sin t)\cos\theta} - \frac{\cos t\tan\theta}{2+\sin t} \tag{11}$$

We also have

$$\phi' = g(t,\theta) = \frac{|\sin\theta|}{(2+\sin t)\cos\theta} \tag{12}$$

The differential equations for the IVP are $\theta' = f(t,\theta)$ and $\phi' = g(t,\theta)$ from Eq. (11) and Eq. (12), respectively.

2.4 Reparametrizing in Terms of s

To reparameterize in terms of s, we set $t = t(s)$ and $\theta(s) = \theta(t(s))$. Differentiating both sides yields $\frac{d\theta(s)}{ds} = \frac{d\theta}{dt}\frac{dt}{ds}$ by the chain rule. Recall that $\frac{dt}{ds} = \cos(\theta)$ and $\frac{d\theta}{dt} = f(t,\theta)$. We find that $\frac{d\theta(s)}{ds} = f(s,\theta)\cos(\theta)$. Using the chain rule to differentiate $\phi(s) = \phi(t(s))$ provides a differential equation for $\frac{d\phi}{ds}$ in a similar manner. The following IVP will be solved in Section 3.

$$\begin{aligned} \frac{d\theta}{ds} &= k_2 + k_3 + \frac{k_2\sin^2(s)}{(2+\sin(s))^2} + \frac{k_1\sin(s)}{2+\sin(s)} - \frac{\cos(s)\sin(\theta)}{2+\sin(s)} \\ \frac{d\phi}{ds} &= \frac{\sin(\theta)}{2+\sin(s)} \\ \theta(0) &= 0 \\ \phi(0) &= 0 \end{aligned} \tag{13}$$

We take $t = \frac{\pi}{2}$ for the initial condition to coincide with the assumptions in [10] that the interface curve starts at the point $(3,0,0)$ and has tangent vector parallel to the z-axis at that point, i.e., $\theta = 0$ when $t = \frac{\pi}{2}$. Since ϕ is the axis rotation angle and no rotation has occurred when $s = 0$, one has $\phi(0) = 0$.

3 Results

Equation (13) is an initial value problem of the form

$$\frac{d\mathbf{y}}{ds} = \mathbf{F}(s,\mathbf{y}), \quad \mathbf{y}(s_0) = \mathbf{y}_0$$

where $\mathbf{y}(s) =< \theta(s), \phi(s) >, \mathbf{F}(s,\mathbf{y}) =< f(s,\theta), g(s,\theta) >$, and $\mathbf{y}(0) = \mathbf{y}_0 =< 0,0 >$. We solve Eq. (13) with MATLAB's *ode45* using a step-size of $h = 0.005$. When $k_3 = 2.3$, we find that 576 steps provides a "curve" that is essentially a full loop, given round-off and accumulated errors. With $h = 0.005$, this implies that $0 \le s \le 2.875$. In the following we supply *ode45* with $0 \le s \le 2.875$ and force all solutions to Eq. (13) to contain 576 points, regardless of k_3 value. We anticipate that future research will relax this restriction.

The dependent variables $\theta_k \approx \theta(s_k)$ and $\phi_k \approx \phi(s_k)$ in Table 1 are obtained from *ode45* using the constants $k_1 = k_2 = 0$ and $k_3 = 2.3$ in order to mimic results in [10]. In our code, we use the approximations

$$\begin{aligned} ds &= h \\ s_k &= s_{k-1} + h \\ dt &= \cos(\theta_k)h \\ t_k &= t_{k-1} + dt \end{aligned}$$

We obtain the red curve in Fig. 3 when graphing the points using MATLAB. Figure 3 includes the curve $x^2 + y^2 = 9$ in black. The numerical solution of Eq. (13), i.e., the

k	s_k	t_k	dt	θ_k	ϕ_k
0	0	1.570796	0.005	0	0
1	0.005	1.575796	0.005	0.011486	0.000014
2	0.01	1.580795	0.004999	0.022943	0.000057
⋮	⋮	⋮	⋮	⋮	⋮
288	1.44	1.637426	-0.004979	3.050090	0.365560
⋮	⋮	⋮	⋮	⋮	⋮
575	2.875	1.567609	0.004960	6.156179	0.027733

$r = 2 + \sin t$	$z = -\cos t$	$x = r\cos\phi$	$y = r\sin\phi$
3	0	3	0
2.999988	0.005	2.999988	0.000043
2.999950	0.009999	2.999950	0.000172
⋮	⋮	⋮	⋮
2.997781	0.066581	2.799699	1.071623
⋮	⋮	⋮	⋮
2.999995	-0.003188	2.998841	0.083188

Table 1: Numerical Solution of IVP Eq. (13)

boundary of the solution patch, is in red. Again, this specific example uses $k_1 = k_2 = 0$ and $k_3 = 2.3$. These specific values were chosen because they correspond to a solution that was presented in [10]. However, [10] also presented solutions for different values of these constants.

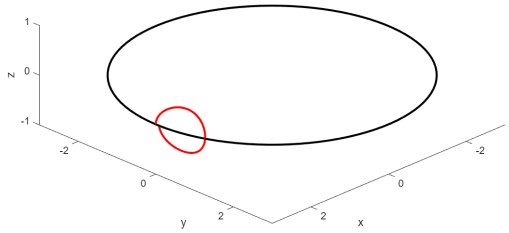

Figure 3: Solution to Eq. (13) with $k_1 = k_2 = 0$ and $k_3 = 2.3$.

3.1 Solutions with Other Values for the Constants

Various values for the constants k_1, k_2, and k_3 can be selected for use in Eq. (13). These different constants correspond to curves found in [10, Fig. 5]. Recall that

$$k_1 = \frac{\Delta\bar{\kappa}}{\sigma} + \frac{\Delta\kappa}{2\sigma}, \quad k_2 = \frac{\Delta\kappa}{4\sigma}, \quad \text{and} \quad k_3 = \frac{\Delta\lambda}{\sigma}$$

and that

$$\eta_k = \frac{\Delta\kappa}{L\sigma} \quad \text{and} \quad \eta_{\bar{k}} = \frac{\Delta\bar{\kappa}}{L\sigma}$$

When choosing values for $\eta_k, \eta_{\bar{k}}$, and $\frac{\Delta\lambda}{\sigma}$ in order to mimic curves from [10, Figure 5], two of the three terms must be zero. To produce curves as in [10, Fig. 5(a)], one can select $\frac{\Delta\lambda}{\sigma}$ and set the other constants to be zero. This is what was done in the first part of Section 3. Since the surface being parametrized is the torus, $L = 3$ was chosen. The reason for this is that L is defined in [10] to be the maximum of $r(t)$. In our case, $r(t) = 2 + \sin(t)$ has a maximum value of 3. Finding appropriate values for k_1 and k_2 to mimic curves in [10, Fig. 5(b)-(c)] is a bit more involved because k_1 and k_2 cannot be selected independently. To do this, k_3 can be taken to be zero, but the equations for the other two constants need to be used in order to get a relation between k_1, k_2, η_k, and $\eta_{\bar{k}}$. Combining all of this, the following is obtained:

$$k_1 = \frac{1}{2}L\eta_k + L\eta_{\bar{k}} \quad \text{and} \quad k_2 = \frac{1}{4}L\eta_k$$

Now, appropriate values for η_k and $\eta_{\bar{k}}$ can be chosen to match [10, Fig. 5(b)] or [10, Fig. 5(c)], which will produce the corresponding values for the constants. Using $L = 3$, we provide two examples in the case where $k_3 = 0$ and $\frac{\Delta\lambda}{\sigma} = 0$.

	$\eta_{\bar{k}}$	η_k	k_1	k_2
Example 1	0	1.85	$\frac{3}{2}(1.85) + 3(0) = 2.775$	$\frac{3}{4}(1.85) = 1.3875$
Example 2	2	0	$\frac{3}{2}(0) + 3(2) = 6$	$\frac{3}{4}(0) = 0$

Table 2: Parameter values for other curves in [10, Fig. 5]

We use *ode45* to solve IVP Eq. (13) with these constants. Plotting the resulting points with MATLAB, the curves in Fig. 4 are obtained. Observe that these curves do not look like the curves seen in [10, Figure 5]. This is expected because the curves in [10] are on a corrugated cylinder instead of a torus. For the remainder of this paper, $k_3 \neq 0$ (and $k_1 = k_2 = 0$) will be the main focus. A future work will consider the more general situation where k_1, k_2, and k_3 could all be nonzero simultaneously.

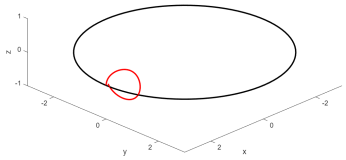

(a) Example 1 solution curve for $\eta_k = 1.85$.

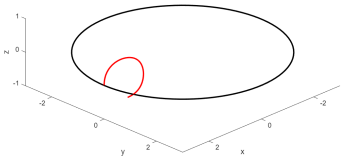

(b) Example 2 solution curve for $\eta_{\bar{k}} = 2$.

Figure 4: Curves found using parameter values from Table 2.

3.2 Setting Up Comparisons Between $E(P_1)$ and $E(P_2)$

Our numerical solver will generate a collection of points that represent the boundary of a patch. However, the patch (and thus its boundary) is not necessarily the only solution to the system. There are other patches that are also solutions to Problem P_i. In particular, since the maximum Gauss curvature of the $(2,1)$-torus is along $x^2 + y^2 = 9$, a disk-like solution could exist at any point on that circle. In order to compare the solutions, it is necessary for $E(P_1)$ and $E(P_2)$ to be "centered" in the same location. To this end, we rotate $E(P_1)$ around the z-axis with a standard rotation matrix:

$$R = \begin{pmatrix} \cos(\Theta) & -\sin(\Theta) & 0 \\ -\sin(\Theta) & \cos(\Theta) & 0 \\ 0 & 0 & 1 \end{pmatrix}$$

The rotation angle Θ is defined below in Eq. (14).

Given a set of points $\{(x_i, y_i, z_i)\}_{i=1}^n \subset \mathbb{R}^3$, the centroid of the set is the point $(\bar{x}, \bar{y}, \bar{z})$ where $\bar{x} = \sum x_i/n, \bar{y} = \sum y_i/n$, and $\bar{z} = \sum z_i/n$. We define Θ to be the angle between the projections of the centroid vectors into the $z = 0$ plane. This will yield two patches whose boundary curves have centroids with equal x and y coordinates. By symmetry, this should also rotate all the other points into their respective spots as the points all have a specific correspondence to the center. Using the points found from both methods, the projected centroid of $E(P_2)$ is

$$\mathbf{C}_2 =< -0.062712, 2.923621, 0 >$$

and the projected centroid of $E(P_1)$ is

$$\mathbf{C}_1 =< 2.870549, 0.574749, 0 >$$

In order to find Θ for use in R, we compute

$$\Theta = \cos^{-1}\left(\frac{\mathbf{C}_2 \cdot \mathbf{C}_1}{||\mathbf{C}_2||\,||\mathbf{C}_1||}\right) = \cos^{-1}\left(\frac{1.500329}{(2.924293)(2.927523)}\right) \tag{14}$$

and thus $\Theta \approx 1.394634$.

Substituting Θ into R, the rotation matrix is found to be

$$R = \begin{pmatrix} 0.175253 & -0.984523 & 0 \\ 0.984523 & 0.175253 & 0 \\ 0 & 0 & 1 \end{pmatrix}$$

This rotation matrix can be used to rotate all the points from one curve towards the other in the usual manner. For example, if $\mathbf{r} =< x, y, z >\in E(P_1)$, its rotated location $< x_{rot}, y_{rot}, z_{rot} >$ is found via the matrix product $R\mathbf{r}^T =< x_{rot}, y_{rot}, z_{rot} >^T$. This allows for an accurate comparison of the two curves. Doing this to all the points in $E(P_1)$ yields the rotated red curve in Figure 5(a). Abusing notation, we will still refer to the rotated set of points as $E(P_1)$. Observe that the two curves are not exactly the same, but this does not mean they are not very close. Different values of k_3 can produce drastically different curves. Figure 5(b) shows a solution curve with $k_3 = 1$. Only using 576 points for the curve is insufficient in this case, but including more points would not make the curve a good approximation to $E(P_2)$. It is now necessary to determine the k_3 value which makes $E(P_1)$ closest to $E(P_2)$. This will be done in Section 3.3.

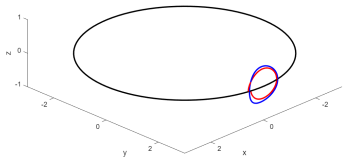

(a) Diffuse interface and rotated IVP curves with $k_3 = 2.3$

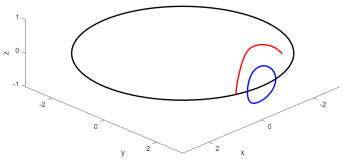

(b) Diffuse interface and rotated IVP curves with $k_3 = 1$

Figure 5: Rotated IVP curves.

3.3 Selecting an Optimal k_3

In order to compare the two boundary curves, a distance between them is computed. Two methods of measuring the distance between two points are geodesic distance and Euclidean distance. Geodesic distance measures the distance between two points restricted to a specified surface by finding the length of the shortest geodesic connecting those points. Euclidean distance measures straight line distance between two points. Given two points (x_1, y_1, z_1) and (x_2, y_2, z_2), the Euclidean distance between them is found using the formula $d = \sqrt{(x_2 - x_1)^2 + (y_2 - y_1)^2 + (z_2 - z_1)^2}$. Geodesic distance is not as simple, as a geodesic has to follow the shape of the surface. Due to its simplicity, Euclidean distance will be used in the comparison of the two solution curves, even though geodesic distance might yield a more accurate comparison. A script in MATLAB will be used to do this for all the points using Euclidean distance. The goal here is to optimize the choice of k_3. This can be done in several different ways. Our procedure in this work

has been to take the boundary curve from the diffuse interface approach as a fixed reference set of points called $E(P_2)$. For exposition, suppose this set of points is labeled as $E(P_2) = \{\mathbf{x}_2^i \mid i = 0, 1, \ldots, 575\}$. By solving Eq. (13), we produce the set of points $E(P_1)$. We can label this set of points as $E(P_1) = \{\mathbf{x}_1^i \mid i = 0, 1, \ldots, 575\}$. By construction, both sets contain 576 points and the sets are naturally ordered so that points can be paired in the sense that the ith point in $E(P_2)$ is approximately the ith point in (the rotated) $E(P_1)$. In this way, for a given value of k_3, one could compute the "paired" distance, d_p, between $E(P_2)$ and $E(P_1)$ as

$$d_p = \min_{0 \le i \le 575} d(\mathbf{x}_2^i, \mathbf{x}_1^i)$$

In this approach, the distance between the curves is 0.0410 when $k_3 = 2.3$. We compute the corresponding "paired" mean squared error as

$$MSE_p = \frac{1}{576} \sum_{i=0}^{575} d(\mathbf{x}_2^i, \mathbf{x}_1^i)^2 = 0.0378$$

In our effort to select an optimal k_3 value, we first select a range of k_3 values from 0.1 to 8, increasing by 0.025 each time. For each of these k_3 values, we compute a value for MSE_p. We find resulting MSE_p values as in Fig. 6(a), and we note that the optimal k_3 value is $k_3 = 2.375$ with $MSE_p = 0.0345$. Fig. 7(a) and Fig. 7(c) show the resulting optimal curve $E(P_1)$ in red.

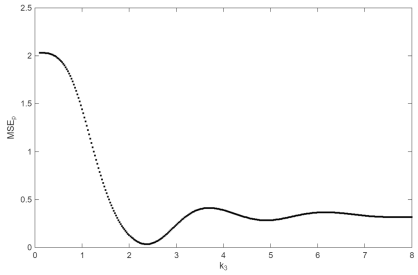

(a) Relationship between k_3 and MSE_p.

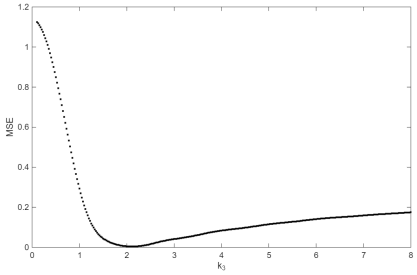

(b) Relationship between k_3 and MSE.

Figure 6: Finding an optimal k_3.

Another approach to computing a distance between $E(P_2)$ and $E(P_1)$ is to compute

$$\min_{0 \le j \le 575} \left\{ \min_{0 \le i \le 575} d(\mathbf{x}_2^j, \mathbf{x}_1^i) \right\}$$

In this approach, the distance between $E(P_2)$ and $E(P_1)$ is 0.0027 when $k_3 = 2.3$. We compute a corresponding MSE in this approach via

$$MSE = \frac{1}{576} \sum_{j=0}^{575} \min_{0 \le i \le 575} d(\mathbf{x}_2^j, \mathbf{x}_1^i)^2 = 0.0072$$

Repeating this computation for $k_3 \in \{0.1, 0.125, \ldots, 8\}$ yields a minimum value of $MSE = 0.0046$ occurring at $k_3 = 2.125$. Figure 6(b) shows all of the MSE values, and Figures 7(b) and 7(d) show the resulting optimal curve $E(P_1)$ in red. The fact that the MSE is so small is a good sign towards saying that our solution to Eq. (13) is similar to $E(P_2)$, i.e., both approaches yield similar results for the phase separation problem.

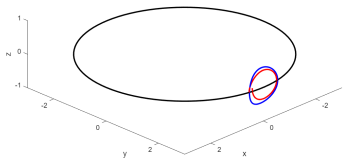

(a) $E(P_1)$ for $k_3 = 2.375$.

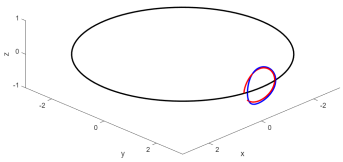

(b) $E(P_1)$ for $k_3 = 2.125$.

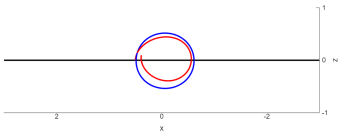

(c) Front view for $E(P_1)$ with $k_3 = 2.375$.

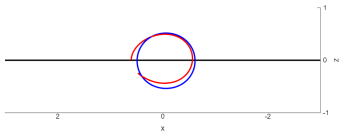

(d) Front view for $E(P_1)$ with $k_3 = 2.125$.

Figure 7: Finding an optimal k_3.

4 Conclusion

This study provides an answer to the question: "How similar are solutions to the phase separation problem from the diffuse interface and IVP approaches?" Grounded in the physical principles of membrane biophysics and the geometric models introduced in [6] and [12], both approaches can be used to understand how curvature and biological conditions interact to organize lipid domains. Using the diffuse interface approach with conservation constraint $\omega = 0.05$, a domain boundary curve was obtained that is consistent with those discussed in [9] and [11]. The IVP approach was constructed from differential equations derived in [10], adapted to the surface geometry of a torus, and then solved using MATLAB's *ode45* solver. In order to obtain a meaningful comparison between the two curves, the centroid of each was computed so that a rotation matrix could be applied to align $E(P_1)$ and $E(P_2)$. Then, the MSE was computed between the curves for incremented values of k_3. The lowest MSE value of 0.0046 was achieved at $k_3 = 2.125$, indicating a close numerical agreement. This result affirms the earlier hypothesis that the two methods yield similar solution curves. We conjecture that improved results, that have less accumulated error, could be obtained in the more general situation where k_1, k_2, and k_3 are all simultaneously nonzero.

The rotational degeneracy, where energy minimizers form along high-curvature loci such as the equator of a torus, is mirrored in the IVP and diffuse interface solutions. By aligning the IVP and diffuse approaches through a rotation, the results confirm not only a numerical alignment between the approaches, but also a deeper structural alignment as well. This was done using a standard rotation matrix, but the Kabsch algorithm explained in [14] could be implemented in future work and might yield better results.

Looking forward, several promising directions emerge. Incorporating geodesic distance in place of Euclidean distance would allow for a more accurate comparison between the curves since the geodesic distance is confined to a given surface. Optimizing additional parameters, exploring alternative parametrizations, and deriving a correspondence between the diffuse interface conservation constraint and the IVP constants will also be investigated. Accomplishing these feats would further strengthen the bridge between these two approaches. Most ambitiously, deriving an analytical solution for a given geometry, when such a solution exists, would give the clearest answer as to how similar these curves are. It would shed light on the solution behavior across different surface geometries.

A Derivation of the Gauss and Mean Curvature

From the literature (see, e.g., [11]) it is known that the solution patch location depends on how the surface is curved. For a given surface M and point in M, take H to be the mean curvature and K to be the Gaussian curvature at the point. Suppose M is an axisymmetric surface parametrized by

$$\mathbf{r}(t,\phi) =< r(t)\cos\phi, r(t)\sin\phi, z(t) >$$

It is well-known (see, e.g., [18, p. 164-165]) that K and H are given by

$$\begin{aligned} K &= \frac{-z'}{r\sqrt{r'^2+z'^2}}\frac{r''z'-r'z''}{(r'^2+z'^2)^{3/2}} \\ H &= \frac{1}{2}\left(\frac{-z'}{r\sqrt{r'^2+z'^2}} + \frac{r''z'-r'z''}{(r'^2+z'^2)^{3/2}}\right) \end{aligned}$$

If the parameter t is chosen to be arc-length, then $r'^2 + z'^2 = 1$. The formulas for K and H simplify to

$$K = -\frac{r''}{r}, \quad H = \frac{1}{2}\left(-\frac{z'}{r} + \frac{r''}{z'}\right)$$

Since $r'^2 + z'^2 = 1$, we introduce an angle $\psi(t)$ so that

$$r' = \cos\psi, \quad z' = \sin\psi$$

Substituting into the formulas for K and H yields

$$K = \frac{\sin\psi}{r}\psi', \quad H = \frac{1}{2}\left(-\frac{\sin\psi}{r} - \psi'\right)$$

which are exactly Eq. (5).

Acknowledgments

The authors thank the Niagara University Honors Program for support during the completion of this work. We also thank the referees for providing valuable suggestions that have greatly improved the exposition.

References

[1] F. Baginski, J. Lu, Numerical investigations of pattern formation in binary systems with inhibitory long-range interaction, *Electron. Res. Arch.*, **30** (2022), 1606–1631.

[2] M. Barg, A. Mangum, Statistical analysis of numerical solutions to constrained phase separation problems, *Electron. Res. Arch.*, **31** (2023), 229–250.

[3] M. Barg, A. Mangum, A phase separation problem and geodesic disks on Cassinian oval surfaces, *Appl. Math. Comput.*, **354** (2019), 192–205.

[4] T. Baumgart, S.T. Hess, W.W. Webb, Imaging coexisting fluid domains in biomembrane models coupling curvature and line tension, *Nature*, **425** (2003), 821–824.

[5] F. Bezzera, L. Santos, A New Look at the Euler-Rodrigues Formula for Three-Dimensional Rotation, *Palest. J. Math.*, **12** (2024), 243–248.

[6] P.B. Canham, The minimum energy of bending as a possible explanation of the biconcave shape of the human red blood cell, *J. Theoret. Biol.*, **26** (1970), 61–81.

[7] R. Choksi, X. Ren, On the derivation of a density functional theory for microphase separation of diblock copolymers, *J. Stat. Phys.*, **113** (2003), 151–176.

[8] C. Elliott, B. Stinner, Surface phase field model for two-phase biological membranes, *SIAM J. Appl. Math.*, **70** (2010), 2904–2928.

[9] F. Baginski , R. Croce , S. Gillmor , R. Krause, Numerical investigations of the role of curvature in strong segregation problems on a given surface, *Appl. Math. Comput.*, **227** (2014), 399–411.

[10] P. Fonda, M. Rinaldin, D.J. Kraft, L. Giomi, Interface geometry of binary mixtures on curved substrates, *Phys. Rev. E.*, **98** (2018).

[11] S. Gillmor, J. Lee, X. Ren, The role of Gauss curvature in a membrane phase separation problem, *Physica D: Nonlinear Phenomena*, **240** (2011), 1913–1927.

[12] W. Helfrich, Elastic properties of lipid bilayers: theory and possible experiments, *Zeitschrift für Naturforschung C*, **28** (1973), 693–703.

[13] F. Jülicher, R. Lipowsky, Domain-induced budding of vesicles, *Phys. Rev. Lett.*, **70** (1993), 2964–2967.

[14] W. Kabsch, A solution for the best rotation to relate two sets of vectors, *Acta Crystallogr. Sect. A*, **32** (1976), 922–923.

[15] U. Seifert, Curvature-Induced Lateral Phase Segregation in Two-Component Vesicles, *Phys. Rep.*, **70** (1993), 1335–1338.

[16] M. Seul, D. Andelman, Domain shapes and patterns: The physics of modulated phases, *Science*, **267** (1995), 476–483.

[17] X. Wang, Q. Du, Modelling and simulations of multi-component lipid membranes and open membranes via diffuse interface approaches, *J. Math. Biol.*, **56** (2008), 347–371.

[18] M. P. do Carmo, *Differential Geometry of Curves and Surfaces*, 2nd edition. Dover Publications, 2016.

Duncan Miller
Rochester Institute of Technology
1 Lomb Memorial Drive
Rochester, NY 14623
E-mail: djm7337@g.rit.edu

Michael Barg
Niagara University
5795 Lewiston Road
Niagara University, NY 14109
E-mail: mbarg@niagara.edu

Received: January 14, 2026 **Accepted**: April 29, 2026
Communicated by Malgorzata Peszynska